

# Flow physics analysis of an auxiliary hole film cooling configuration : Part 1 - Experimental investigation using phosphor thermometry

**Arunprasath Subramanian**

Research scholar,  
Institut P'  
ISAE-ENSMA  
Poitiers, France 86000  
Email: arunprasath.subramanian@ensma.fr

**Gildas Lalizel**

Assistant professor  
Institut P'  
ISAE-ENSMA  
Poitiers, France 86000  
Email: gildas.lalizel@ensma.fr

**Eva Dorignac**

Professor  
Institut P'  
Department of Fluid, Thermal and Combustion(FTC)  
University of Poitiers  
Poitiers, France 86000  
Email: eva.dorignac@univ-poitiers.fr

**Patrick Berterretche**

Research engineer  
Institut P',CNRS  
Poitiers, France 86000

*Film cooling techniques have been employed in turbine blades so that the high temperature and mechanical loads do not trigger the failure of the material. Even with the advancements in the materials used in turbine blades, it is imperative to improve cycle efficiencies in every aspect in order to meet the emission goals set by governments across the world. This work is aimed at understanding a recent unconventional film cooling hole configuration called the auxiliary hole configuration and is presented in two parts. This current article presents the experimental results of the film cooling study using ZnO phosphor thermometry. An auxiliary hole configuration is analysed and compared with a simple cylindrical hole. A cold jet with a blowing ratio of  $M=3$  at  $20^\circ\text{C}$  is injected at an angle in a crossflow at  $150^\circ\text{C}$  and a mass flow rate of  $1\text{kg/s}$ . 2-D flow field temperature contours have shown improvements in the lateral and flow-wise directional superiority of the auxiliary hole film cooling configuration as compared to a simple cylindrical hole.*

## NOMENCLATURE

$\eta$	Adiabatic film effectiveness
$\phi$	Non-dimensional wall temperature
$\theta$	Non-dimensional film temperature
$d$	Diameter of auxiliary hole
$D$	Diameter of main hole
$D_1$	Diameter of single hole
$T_i$	Injected jet temperature
$T_w$	Wall temperature
$T_{aw}$	Adiabatic wall temperature
$T_\infty$	Freestream temperature
$U_i$	Injected jet velocity
$U_x$	x-component velocity
$U_0$	Freestream velocity

## 1 INTRODUCTION

In the recent times, there is an increased emphasis on reducing the gaseous emissions especially in the aviation sector. In this regard, the gas turbine engine cycle efficiencies are required to be at their highest so as to reduce the fuel consumption and hence the emissions. In

the quest for higher working efficiency, cooling strategies have been employed in the combustion chamber and the turbine blades so as to improve the Turbine Inlet Temperature (TIT), due to the fact that combustion at higher temperatures yield higher efficiency. One of the cooling strategies currently in use is film cooling, which employs a film of air covering the surface to be cooled so as to reduce the heat transfer into the surface, turbine blade for example. Over the years various studies have been conducted to study the effect of hole shapes, arrangement of holes, density ratio, blowing ratio, and other factors [1].

Film cooling applications involve a phenomena called the Jet in cross flow (JICF) where a coolant jet is injected across a wall into a mainstream flow. Such a flow is observed in many other cases like a chimney or volcanic eruption too. The aerodynamic consequences due to the interaction of the jet with the cross-flow are many and it is important to understand the flow structures that evolve around the jet. In this section a brief explanation of the coherent structures formed due to the JICF is discussed. Depending on the velocity at which the jet is injected into the mainstream flow, different flow regimes are obtained, due to the trajectory of the jet. The basic idea of film cooling is to have a good film coverage over the surface of the turbine blade or the combustion chamber liner and hence, we need to define the regimes at which the flow stays close to the wall. Figure 1 shows a classical JICF arrangement.

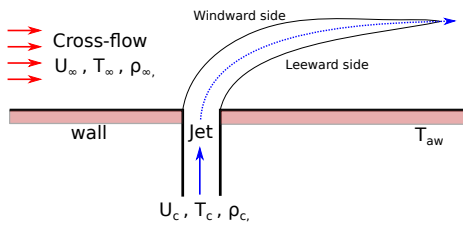


Fig. 1. Arrangement of a Jet In Cross-Flow system.

In the recent past, improvements in additive manufacturing and the improvements in precision engineering have paved the way to make finer and complex hole shapes. The shape of the hole and its characteristics like the channel angle, hole exit angle, orientation of the hole with respect to the axis of the crossflow have a profound effect on the flow structures downstream of the hole exit. Various complex hole shapes have been proposed and analysed (Fan shaped by [2], crescent [3], ramp by [4]

, slot cooling by [5], effusion cooling by [6]) other than usual cylindrical hole shapes ([7],[8]) with the aim to improve the film cooling efficiency through reduction in the CRVP intensity and height. Despite this, primitive hole shapes are preferred so as to reduce the manufacturing costs involved in producing complex shapes and to facilitate easier maintenance of the turbine blades once in service.

The system of a cylindrical hole with auxiliary holes or 'sister holes' arrangement was proposed in the 2000s by [9]. Since then few number of numerical studies have been done on such an arrangement where a main hole is supported by two smaller holes upstream or downstream ([10],[11], [12], [13]). The understanding from these works is that the efficiency of the sister hole arrangement is improved immensely comparing with a simple single hole geometry. However, since most of the studies are numerical analyses alone, there is a need for experimental test data. In this article, phosphor thermometry is employed to test this novel hole arrangement so as to visualise the 2-D temperature field.

## 1.1 Objectives of this study

This work aims to establish the working of the auxiliary hole film cooling configuration which has the potential to improve film cooling efficiency without requiring much improvements in machining techniques.

- Phosphor thermometry using ZnO particles set-up to visualise the 2-D temperature flow fields in film cooling arrangements
- Study the flow fields in a simple cylindrical hole arrangement and auxiliary hole arrangement along the flow direction and the spanwise direction.
- Instantaneous and average temperature flow-field data to compare with time-resolved numerical simulations (described in part II of this work) to provide a comprehensive data to analyse the CRVP systems in the two hole configurations.

## 2 EXPERIMENTAL SETUP

### 2.1 Description of test bench

The BATH test bench is an open circuit wind tunnel which aims to recreate the flow and temperature conditions found in aero engines within a test section. Air from a compressor tank is electrically heated before controlled air-kerosene combustion which raises the temperature of the air to extreme temperatures. It consists of a premix chamber where kerosene is injected and vaporized into an air flow, a combustion chamber fitted with a spark plug, a two-stage dilution chamber where a flow of fresh air is

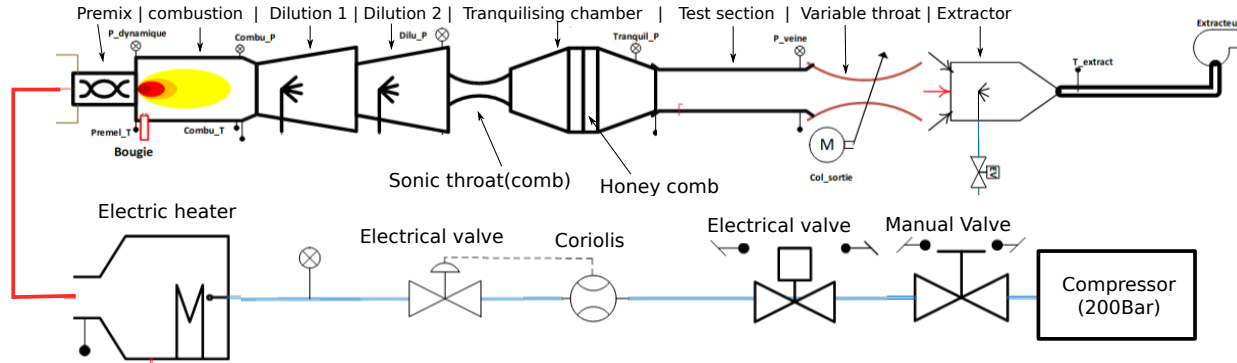


Fig. 2. Schematic view of the Bath test rig components

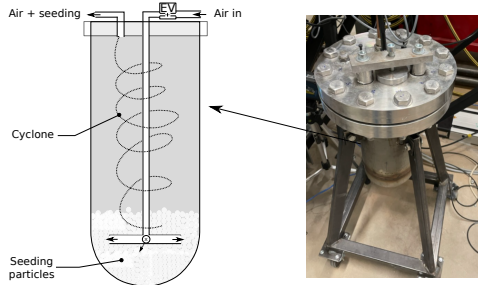


Fig. 3. Picture showing the seeding chamber with supports.

added, a sonic-throat which ensures a constant flow in the test section and a convergent-divergent chamber which dampens the turbulence of the flow. Moreover, this also helps in increasing the pressure in the combustion chamber and a lower pressure in the test section at high mass flow rates. An adjustable neck at the test section outlet makes it possible to adjust the pressure in the test section. At the outlet of the test channel, the flow is taken up by an extractor which expels the flow outside the building. This flow is diluted with the air from the test hall and is cooled by spraying water.

The seeding system is seen in figure 3 which can be filled with common seeding particles like  $SiO_2$  or phosphor particles like  $ZnO$ . The final design of the seeding pot was conceived after many iterations and modifications of the air feed tube to obtain good feeding by reduced particle agglomeration and increased particle fluidity.

The boundary conditions of the film cooling arrangement are shown in table 1. Electrically heated air at  $150^\circ C$  is fed in the crossflow at a mass flow rate of  $300g/s$ . A seeding chamber as described before helps in infusing  $ZnO$  phosphor particles in the flow. Film cooling holes are connected to a separate seeding chamber which is fed with a constant mass flow rate of  $4.45g/s$  thanks to an ori-

fice tube which ensures constant a mass flow rate. This air is maintained at  $20^\circ C$ , which leads to a blowing ratio of  $M=3$ . The reason for choosing a higher blowing ratio is the high jet penetration which makes the visualisation of the 2-D temperature field all along the jet trajectory achievable. Additionally, the coherent structures are amplified and helps in better identification and quantification.

Table 1. Boundary conditions

Parameter	Cross-flow	Jet
Mass flow	$310g/s$	$4.45g/s$
Temperature	$150^\circ C$	$20^\circ C$
Density	$0.83kg/m^3$	$1.32kg/m^3$
Pressure	$1.2bar$	$1.2bar$
Velocity (theoretical)	$12.8m/s$	$27.5m/s$
Blowing ratio 'M'		3
Density ratio		1.45

## 2.2 Film cooling geometry

In this section, the film configurations are described. In order to have preliminary verification that the proposed auxiliary hole configurations have favourable flow characteristics, a case with cylindrical hole is used as a reference. Table 2 shows the various geometrical characteristics of the two configurations studied.

Figure 4 is a representation of the film cooling module. It must be noted that although experiments are conducted at relatively lower temperatures ( $150^\circ C$  in the mainstream flow) in this work, the test bench is capable

Table 2. Geometric parameters

Parameter	Single hole	Aux. hole case
Main hole Diameter	$D_1=12.25$ [mm]	$D=10$ [mm]
Aux. hole Diameter	-	$d=5$ [mm]
Aux. hole lateral distance	-	$H=15$ [mm]
Aux. hole longitudinal distance	-	$L=15$ [mm]

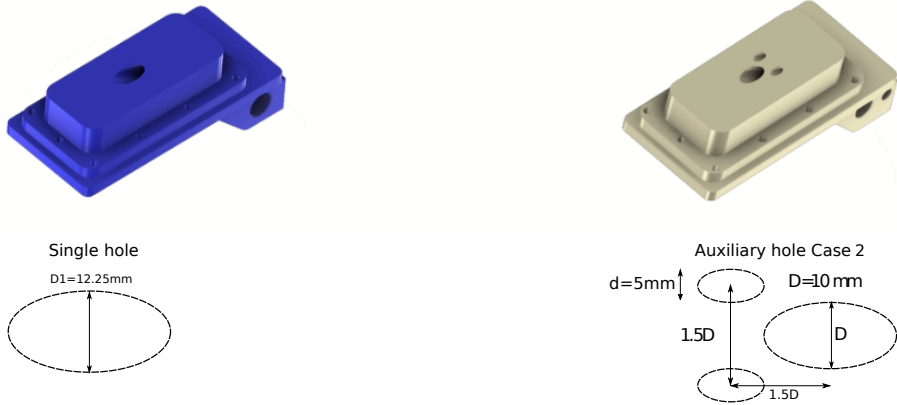


Fig. 4. Illustration of the film cooling modules used in this work and their corresponding hole shape from the top view is shown below each module with geometrical parameters.

of performing film cooling analysis at very high temperatures of the order of  $1500^{\circ}\text{C}$  at 10 bars of pressure. This is the reason for the film cooling modules and the other surfaces to have a thick wall.

### 3 PHOSPHOR THERMOMETRY SETUP

The use of phosphor thermometry is a novelty in analysing the film cooling physics in this work. A short description of the spectral intensity ratio method and the properties of ZnO phosphor are presented. Additionally, an overview of the various components necessary to acquire the images are described in this section. A more detailed explanation is provided in a separate article on ZnO phosphor thermometry [14].

#### 3.1 Spectral intensity ratio method

The phosphor particles absorb the incident radiation  $I_0$  and get excited to higher temporary energy states. They return to the lower energy states by emission of radiation, and for the purpose of phosphor thermometry, phosphors with emission in the visible spectrum are preferred. The number of photons emitted upon excitation by a laser depends on various factors like temperature of the working

fluid  $T$ , the local concentration  $\chi$  of particles, the laser sheet intensity  $I_0$  working at wavelength  $\lambda_0$  and the inherent emission property of the phosphor used  $\sigma$ . The emission intensity  $I$  is given by the expression:

$$I(\lambda, x, y, z) \approx \underbrace{I_0(\lambda_0, x, y, z)}_{(1)} \underbrace{\sigma(\lambda_0, T)}_{(2)} \underbrace{\exp(\chi(x, y, z)d)}_{(3)} \underbrace{\chi(x, y, z)}_{(4)} \quad (1)$$

In the above equation the emission intensity hence depends on (1) laser wavelength and intensity, (2) phosphor characteristics, (3) the local absorption due to Beer-Lambert effect and (4) local concentration of phosphor particles. In addition to these parameters, factors like detector efficiency, the transitivity of optics and the direction at which the radiation is emitted upon excitation also play a role on the detected emission intensity.

Spectral intensity ratio method: By observing the phosphor emission through two different wavelength bandwidths by use of filters, the division of the two filtered images can be effectively used to calibrate tempera-

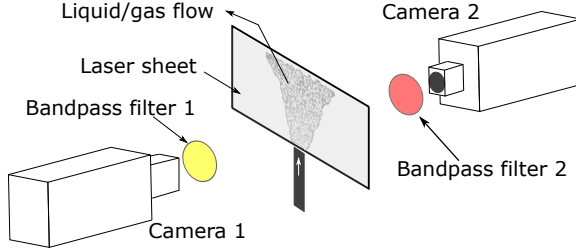


Fig. 5. Spectral intensity ratio method: A typical experimental setup.

tures (Refer figure 5). However, due to the use of filters, the collection of the emission signal is drastically reduced and some times necessitates the need for an intensified camera.

As the spectroscopic distribution changes, the relative intensity of some of the emission bands varies in relation to one another. By collecting the emission intensity of each of the two bands by means of a 2-D detector, such as an ICCD camera, the intensity ratio at a specific temperature can be obtained. By changing the temperature of the phosphor, full temperature calibration of this ratio can be achieved.

From eq. 1 it can be seen that the emission dependence on the laser wavelength, local Beer-Lambert absorption and the local concentration of the particles can be eliminated, if the intensity of emission emitted by a phosphor particle at different wavelengths can be divided by one another.

$$\frac{S_{\lambda_1}}{S_{\lambda_2}} = \frac{\sigma(\lambda_0, T_1)}{\sigma(\lambda_0, T_2)} \quad (2)$$

From eq. 2, it can be seen that by such a division, the intensity ratio value depends only on the temperature of the phosphor and the excitation source wavelength.

There are several setup configurations that can be used to determine temperatures by use of the intensity ratio method. The first of these involves use of two cameras, each equipped with an interference filter that transmits one of the bands of the emitted radiation and blocks the others. This configuration requires spatial matching of the two detectors in order to obtain an accurate two-dimensional temperature map. The second configuration utilizes a stereoscope fitted to a single camera which enables the projection of the spectral intensity of each band onto a single detector chip. Stereoscopes can suffer from radiation cross-talk which can affect the accuracy of the temperature determination obtained though.

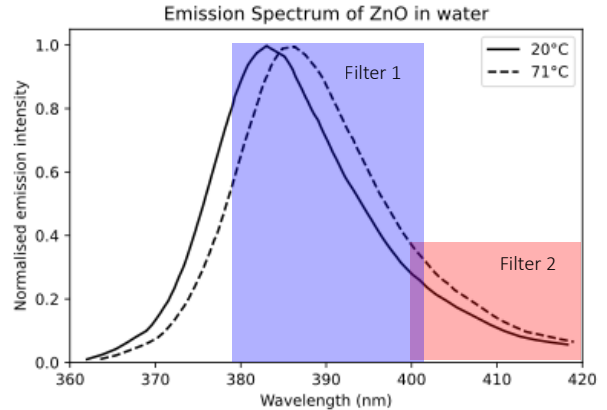


Fig. 6. Emission spectrum of ZnO in water at two different temperatures. The filters used in this study are overlaid for reference.

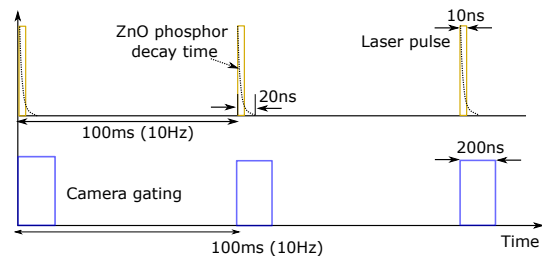


Fig. 7. Timing and synchronisation diagram showing the camera and laser firing.

### 3.1.1 Excitation source: Laser

A Quantel Q-smart 850 laser was used as the laser for the PIV analysis. The laser works at a constant frequency of 10 Hz with a pulse duration of about 6ns. The energy obtained from this laser is 100mJ is sufficient enough to perform phosphor thermometry as the energy density of this laser is 50mJ/cm<sup>2</sup> which is in the luminescence emission saturated regime [15].

### 3.1.2 Camera

The ANDOR iStar sCMOS camera is used due to the advantage of an intensifier and the short gating widths (in the order of ns) possible with this camera. The high resolution of the ANDOR camera permits us to capture the nuances of the instantaneous flow field despite these averaging processes. For each calibration point and ensuing film cooling study case, 150 images were obtained by capturing images at 10Hz and with a gating width of 200ns and camera gain of 2000. Figure 7 shows the timing diagram of the current setup.

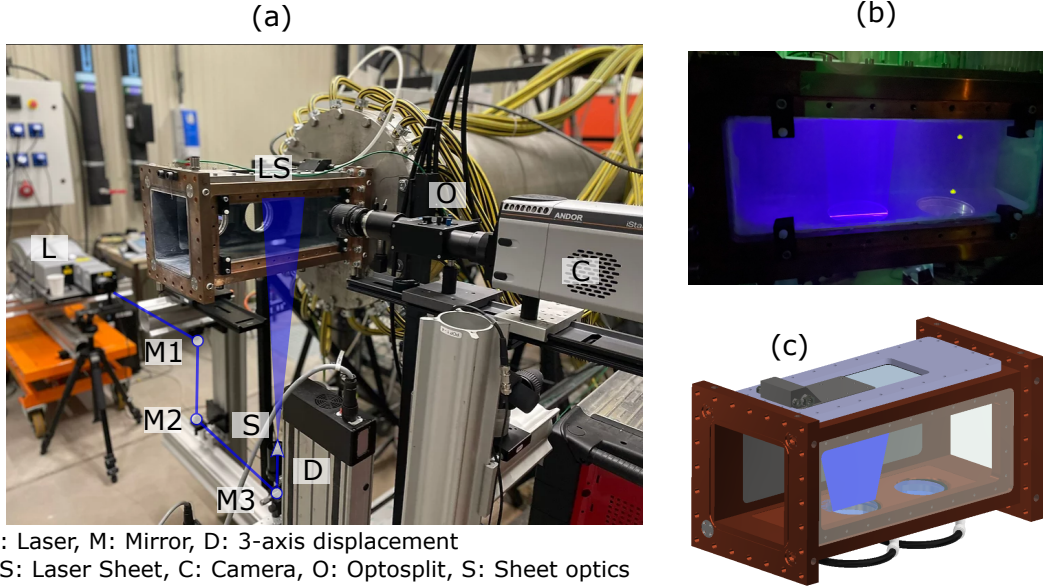


Fig. 8. (a) Illustration of the PIV/ phosphor thermometry setup. (b) Actual image of the inside of the test section during the phosphor thermometry image acquisition. (c) CAD illustration of the laser path in the test section

### 3.1.3 Optics

Figure 8 shows the arrangement of the various components related to the image acquisition. Owing to the difficulty to placing the laser beneath the test section, relay mirrors are used to reflect the 266nm laser beam up to the laser sheet generator placed directly below the test section. A laser sheet generator is used to create the laser sheet of thickness which is less than 0.5mm at the entrance of the test section's optical access.

A thin laser sheet helps in eliminating three dimensional particle effects as the flow in the current configuration (film cooling) is very much three dimensional. As can be observed, an Optosplit II device is used in front of the camera so as to be able to perform the spectral intensity ratio method using a single camera.

The Optosplit as shown in the figure 9 is used to separate incident emission radiation from the ZnO into two paths, with each passing through a bandpass filter. After passing through the filters, these two paths are 're-paralleled' to form two images of the same region of interest on the same image frame. The choice of filters, objective lenses used are mentioned in the table 3. A larger bandwidth for the filters was selected than the previous studies [16] to allow more incident light on the camera.

### 3.2 Calibration

The calibration procedure starts with the acquisition of the intensity images of the two spectral bands that have

been pre-selected by the user. Then, the images are subjected to background subtraction and to de-warping process to adjust image distortions. After this the division of the two intensity maps results in the intensity ratio distribution corresponding to the temperature distribution of the object. The intensity ratio distribution obtained is then transformed into temperature values by use of a calibration polynomial to convert the ratios obtained.

At least 7 calibration points were chosen to obtain the intensity ratio vs temperature calibration curve as shown in the figure 10. The images acquired were applied with a moving Gaussian filter (3x3 pixels) and binned (5x5 pixels) using python code developed in-house.

## 4 RESULTS

Both the configurations were tested at a blowing ratio of 3 owing to the simplicity in capturing the flow field far away from the wall. This is preferred as the ZnO particle deposition on the walls can cause bright zones just above the wall which lead to non-physical results. Low blowing ratio flows are restricted to short heights over the wall and hence limit the visualisation. In this section, the 2-D temperature visualisation results are presented for the baseline case (single hole case) and the auxiliary hole case. The different planes along the Y-direction are analysed so as to get a better view of the lateral spread of the film cooling jet. The 2-D non-dimensional temperature ( $\theta$ ) fields obtained from the film cooling experiments are discussed.

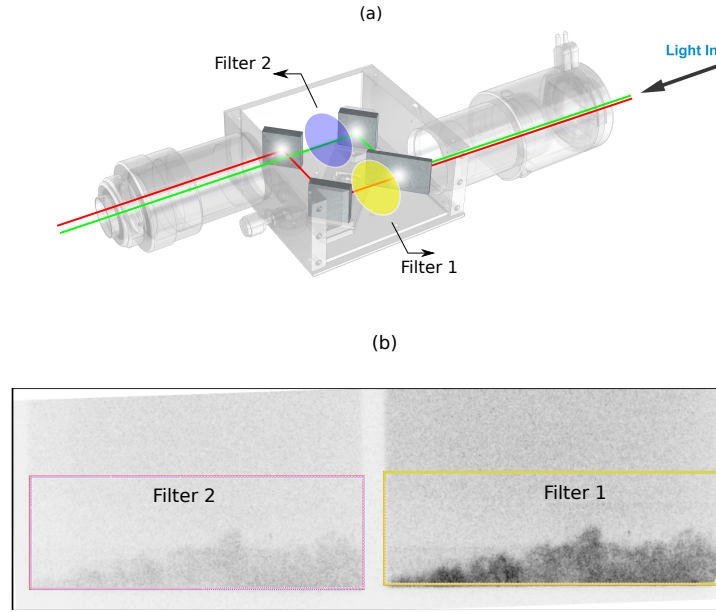


Fig. 9. (a) Schematic representation of the working of optosplit device. (b) Raw image obtained on the ANDOR camera with two filtered images of the ZnO emission obtained during film cooling experiments.

Table 3. Lens and filters used

Part	Brand	Model	Characteristics
Objective lens	Nikon	AF Nikkor 28mm f/2.8D	Minimum aperture f/2.8
Bandpass filter	Chroma	ET395/25x	(395/25nm)
Bandpass filter	Chroma	AT425/50x	(425/50nm)

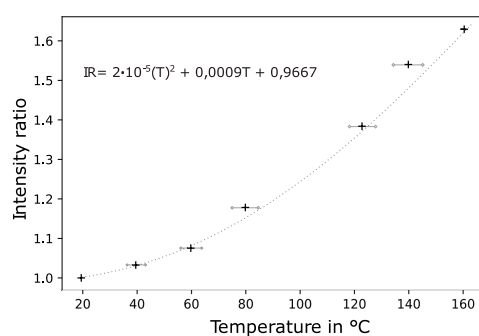


Fig. 10. Intensity ratio vs temperature calibration curve for the ZnO phosphor in air.

$$\theta = \frac{T_\infty - T}{T_\infty - T_c} \quad (3)$$

#### 4.1 Single hole configuration

Figures 11, 12, 13 show the 2-D non-dimensional temperature fields for the single hole case at  $Y/D=0$ ,  $Y/D=0.4$ ,  $Y/D=0.8$  respectively. The regions marked in blue indicate the presence of jet flow and the regions marked in red indicate mainstream flow and any color in between highlights the mixing between the jet and mainstream flows.

In figure 11, (a) shows the mean flow field and (b-d) show the instantaneous flow field obtained at different instances at  $Y=0$  (centerline). The mean flow field are obtained by simply averaging the instantaneous images. From 11(a), one can clearly observe the trajectory of the film cooling jet as well as the prominent  $\theta$  contours. The jet penetrates into the mainstream flow and has enough momentum to remain detached from the wall. In 11 (b), (c), (d) the instantaneous images help in identifying the jet-shear layer vortices in the top and the bottom areas of

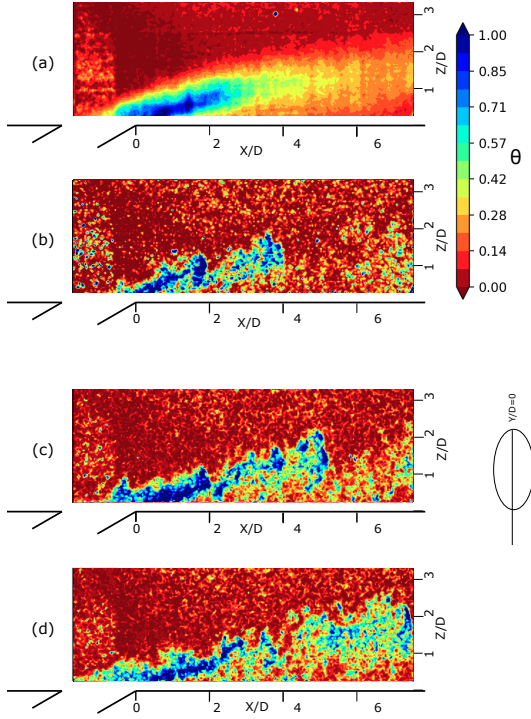


Fig. 11. Phosphor thermometry: Non-dimensional temperature contours for  $M=3$  for single hole case at  $Y/D=0$ . (a) Mean flow field. (b-d) instantaneous flow fields at different instances.

the jet. Additionally, it can be seen that the jet initially penetrates into the mainstream and later becomes unstable upon interaction with the main flow and 'packets' of cold air mix with the mainstream further downstream.

Similarly, in figure 12, (a) shows the mean flow field and (b-d) show the instantaneous flow field obtained at different instances at  $Y/D=0.4$ . It can be noticed that the strength of the jet core is reduced as compared to the case  $Y/D=0$ . The instantaneous flow fields show the wavy motion of the jet, which mixes with the mainstream all along the direction of the flow.

Figure 13(a) shows the mean flow field and (b-d) show the instantaneous flow field obtained at different instances at  $Y/D=0.8$ . The mean flow field (figure (a)), highlights the fact that at the outer edge of the film cooling hole, the high shear and mixing with the main flow starts much earlier leading to the reduced film presence. The instantaneous snapshots of the flow field show very few packets of film cooling jet in the mainstream flow showing the edges of the Kelvin-Helmholtz vortices.

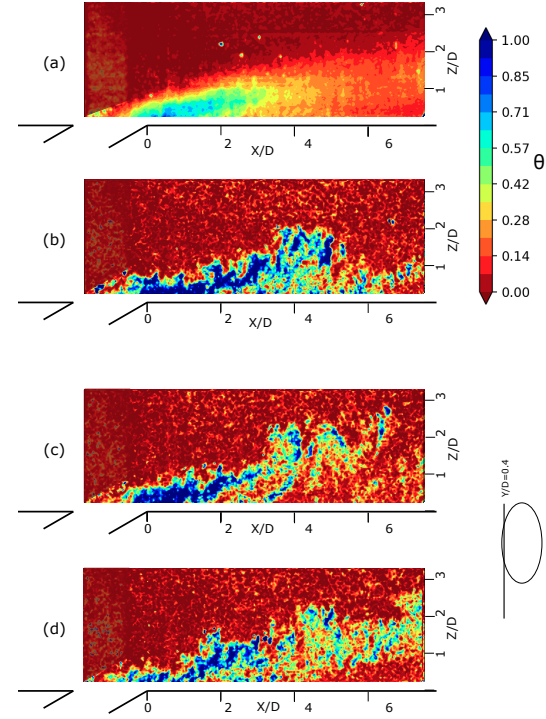


Fig. 12. Phosphor thermometry: Non-dimensional temperature contours for  $M=3$  for single hole case at  $Y/D=0.4$ . (a) Mean flow field. (b-d) instantaneous flow fields at different instances.

#### 4.2 Auxiliary hole configuration

The auxiliary hole case presents interesting 2-D temperature contour results. Figures 14-16 show the non-dimensional temperature contour at various lateral locations as discussed earlier. (a) shows the mean flow field and (b-d) show the instantaneous flow field obtained at different instances.

Figure 14 shows the non-dimensional temperature contour at  $Y/D=0$  (centerline). The first observation of figure 14 (a) highlights the tendency of the jet flow to be closer towards the wall than that of the single hole case (refer figure 11 (a)). Similar to the single hole case, the jet flow throws out packets of cold air that mix with the main flow further downstream. The intensity of the mixing and the corresponding vortex intensities and velocities can be visualised by LES numerical analyses.

Figure 15 shows the most interesting results with the presence of a secondary streak above the main hole jet. This streak could arise due to the presence of the auxiliary holes upstream of the main hole. The flow from the auxiliary hole in this case essentially reduces the shear experienced by the jet due to contact with the main flow.

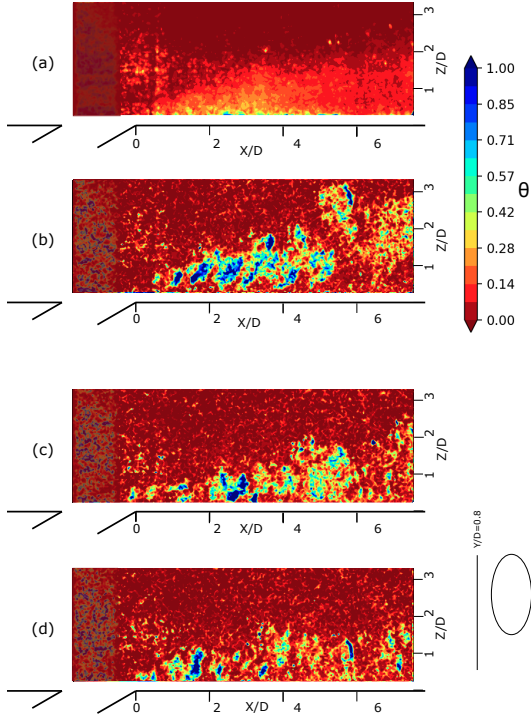


Fig. 13. Phosphor thermometry: Non-dimensional temperature contours for  $M=3$  for single hole case at  $Y/D=0.8$ . (a) Mean flow field. (b-d) instantaneous flow fields at different instances.

At  $Y/D=0.4$ , there is an increased jet presence in the flow field, due to the effect of the auxiliary holes. From the instantaneous images (b-d) one can also observe that the jet travels longer distance before dissipation into the main flow as compared to the single hole case.

Figure 16 shows the contour plots for non-dimensional temperature at  $Y/D=0.8$ . The jet-shear layer vortices or the tornado vortices can be very clearly identified from the instantaneous snapshots. Additionally, the mean flow field highlights improved jet presence as compared to the single hole case as seen in the figure 13.

Similar to the trends seen at other  $Y$  locations,  $\theta$  contours show that the auxiliary hole case presents jet flow even at locations  $X/D < 2$  which was unseen in the single hole case at similar  $Y$  location. Hence the Auxiliary hole configuration definitely has better lateral spread characteristics than the single hole case. Comparing figure 12 and figure 16 which are locations at the edge of the hole arrangements, one can notice that the auxiliary hole case configuration shows a lift-off compared to the single hole case which stays closer to the wall. In order to understand this phenomenon more in detail, it is necessary to observe 3-D flow structures, which is possible through large eddy

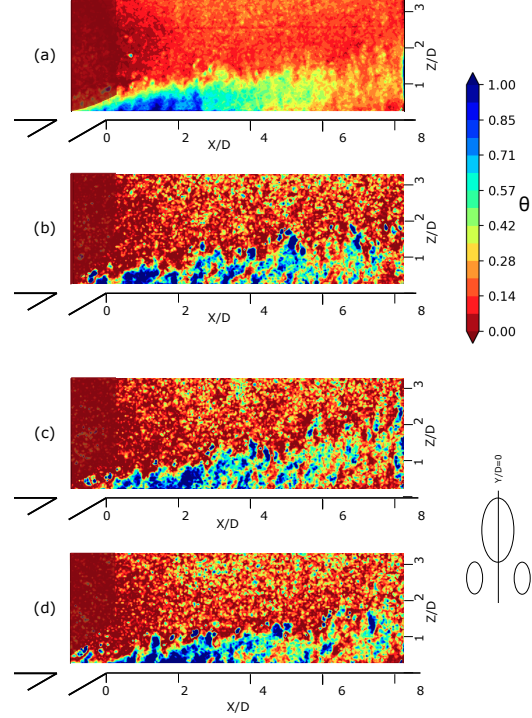


Fig. 14. Phosphor thermometry: Non-dimensional temperature contours for  $M=3$  for Auxiliary hole case at  $Y/D=0$ . (a) Mean flow field. (b-d) instantaneous flow fields at different instances.

simulations (LES). A clear description of this flow structure is provided in the second part of this study.

Despite this, it is evident that the visualisation of the temperature flow field using phosphor thermometry is highly beneficial to the better understand of the film cooling process as it allows comparison between different film cooling configurations, and identification of coherent structures.

## 5 CONCLUSION

In this article, the new BATH test rig where the film cooling study is conducted has been described. ZnO phosphor thermometry was successfully implemented to study film cooling configurations in this test bench. A cold jet seeded with ZnO particles was injected in a main seeded crossflow at  $150^{\circ}\text{C}$  with a blowing ratio  $M=3$ . This blowing ratio was used due to the better visualisation possible due to high penetration of the injected cold jet. High resolution 2-D temperature contour results were obtained through a series of experiments for the three test cases. The key learning from this study was that the auxiliary hole system has very favourable flow characteristics as compared to the single hole case, as the cold jet stays

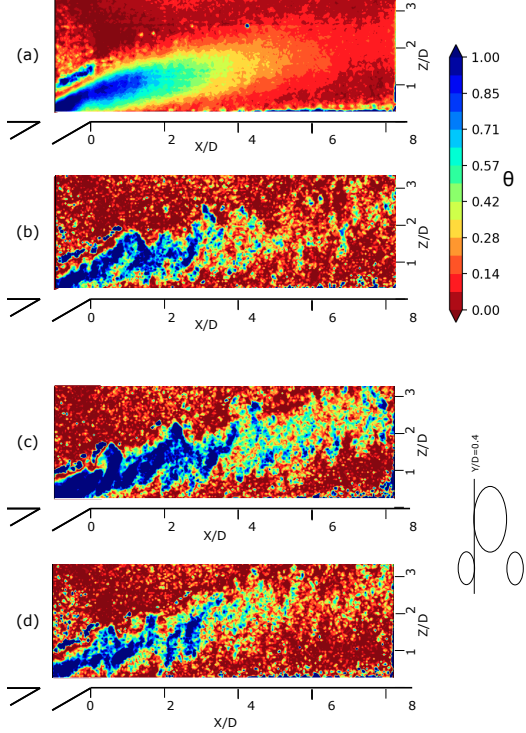


Fig. 15. Phosphor thermometry: Non-dimensional temperature contours for  $M=3$  for Auxiliary hole case at  $Y/D=0.4$ . (a) Mean flow field. (b-d) instantaneous flow fields at different instances.

closer to the wall. Additionally, the injected jet in the auxiliary hole case has a greater lateral spread ( $Y/D \approx 0.8$ ) than that of the single hole case ( $Y/D \approx 0.4$ ). The possibility of identifying key coherent structures like the jet-shear layer vortices show the fidelity of the phosphor thermometry technique. In order to understand these complex 3-D structures observed in experiments, Large Eddy Simulations can provide better insights.

## 6 ACKNOWLEDGEMENTS

This work was partially funded by the French Government program “Investissements d’Avenir” (EQUIPEX GAP, reference ANR-11-EQPX-0018).

## REFERENCES

- [1] Bunker, R. S., 2005, “A review of shaped hole turbine film-cooling technology,” *J. Heat Transfer*, **127**(4), pp. 441–453.
- [2] Gritsch, M., Colban, W., Schär, H., and Döbbeling, K., 2005, “Effect of hole geometry on the thermal performance of fan-shaped film cooling holes.”
- [3] Dai, P., and Lin, F., 2011, “Numerical study on film cooling effectiveness from shaped and crescent holes,” *Heat and mass transfer*, **47**(2), pp. 147–154.
- [4] Barigozzi, G., Franchini, G., and Perdichizzi, A., 2007, “The effect of an upstream ramp on cylindrical and fan-shaped hole film cooling: Part ii—adiabatic effectiveness results,” In *Turbo Expo: Power for Land, Sea, and Air*, Vol. 47934, pp. 115–123.
- [5] Sargison, J., Guo, S., Oldfield, M., Lock, G., and Rawlinson, A., 2002, “A converging slot-hole film-cooling geometry—part 1: low-speed flat-plate heat transfer and loss,” *J. Turbomach.*, **124**(3), pp. 453–460.
- [6] Lenzi, T., Palanti, L., Picchi, A., Bacci, T., Mazzei, L., Andreini, A., and Facchini, B., 2020, “Time-resolved flow field analysis of effusion cooling system with representative swirling main flow,” *Journal of Turbomachinery*, **142**(6).
- [7] Lutum, E., and Johnson, B. V., 1999, “Influence of the hole length-to-diameter ratio on film cooling with cylindrical holes.”
- [8] Walters, D. K., and Leyklek, J. H., 2000, “A detailed

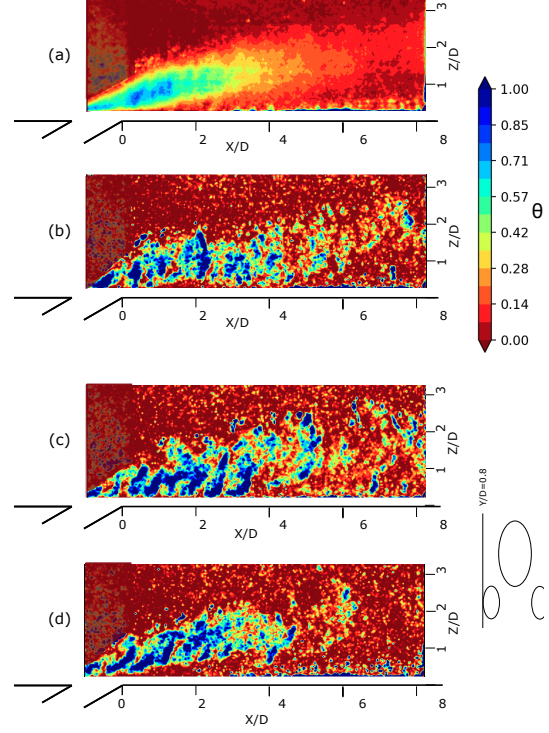


Fig. 16. Phosphor thermometry: Non-dimensional temperature contours for  $M=3$  for Auxiliary hole case at  $Y/D=0.8$ . (a) Mean flow field. (b-d) instantaneous flow fields at different instances.

- analysis of film-cooling physics: part i—streamwise injection with cylindrical holes,” *J. Turbomach.*, **122**(1), pp. 102–112.
- [9] Heidmann, J. D., and Ekkad, S., 2008, “A novel antivortex turbine film-cooling hole concept,” *Journal of turbomachinery*, **130**(3).
  - [10] Ely, M. J., and Jubran, B., 2008, “A numerical study on increasing film cooling effectiveness through the use of sister holes,” In *Turbo Expo: Power for Land, Sea, and Air*, Vol. 43147, pp. 341–350.
  - [11] Ely, M. J., and Jubran, B., 2009, “A numerical evaluation on the effect of sister holes on film cooling effectiveness and the surrounding flow field,” *Heat and Mass Transfer*, **45**(11), pp. 1435–1446.
  - [12] Park, S., Chung, H., Choi, S. M., Kim, S. H., and Cho, H. H., 2017, “Design of sister hole arrangements to reduce kidney vortex for film cooling enhancement,” *Journal of Mechanical Science and Technology*, **31**(8), pp. 3981–3992.
  - [13] Zhou, J., Wang, X., Li, J., and Lu, H., 2020, “Effects of diameter ratio and inclination angle on flow and heat transfer characteristics of sister holes film cooling,” *International Communications in Heat and Mass Transfer*, **110**, p. 104426.
  - [14] Arunprasath Subramanian, L., and Dorignac, E. “Zno phosphor thermometry in water: Novel temporal method using rise time-decay time ratio,” *Submitted article to Measurement science and technology journal*.
  - [15] Abram, C., Fond, B., and Beyrau, F., 2015, “High-precision flow temperature imaging using zno thermographic phosphor tracer particles,” *Optics express*, **23**(15), pp. 19453–19468.
  - [16] Abram, C., Pougin, M., and Beyrau, F., 2016, “Temperature field measurements in liquids using zno thermographic phosphor tracer particles,” *Experiments in Fluids*, **57**(7), p. 115.